PAPER • OPEN ACCESS

Quantum multicritical behavior for coupled optical cavities with driven laser fields

To cite this article: Yutao Hu *et al* 2023 *New J. Phys.* **25** 053001

View the article online for updates and enhancements.

New Journal of Physics

The open access journal at the forefront of physics

PAPER

Quantum multicritical behavior for coupled optical cavities with driven laser fields

Yutao Hu[1], Yu Zhou[2], Wenchen Luo[1,*], Andrea Trombettoni[3,5,6] and Guoxiang Huang[4,7,8]

[1] School of Physics and Electronics, Central South University, Changsha 410083, People's Republic of China
[2] School of Science and Shenlan College, Jiangsu University of Science and Technology, Zhenjiang, Jiangsu 212003, People's Republic of China
[3] Department of Physics, University of Trieste, Strada Costiera 11, I-34151 Trieste, Italy
[4] State Key Laboratory of Precision Spectroscopy, East China Normal University, Shanghai 200062, People's Republic of China
[5] SISSA and INFN, Sezione di Trieste, Via Bonomea 265, I-34136 Trieste, Italy
[6] CNR-IOM DEMOCRITOS Simulation Center and SISSA, Via Bonomea 265 I-34136 Trieste, Italy
[7] NYU-ECNU Joint Institute of Physics at NYU-Shanghai, Shanghai 200062, People's Republic of China
[8] Collaborative Innovation Center of Extreme Optics, Shanxi University, Taiyuan, Shanxi 030006, People's Republic of China
* Author to whom any correspondence should be addressed.

E-mail: luo.wenchen@csu.edu.cn

Abstract

Quantum phase transitions with multicritical points are fascinating phenomena occurring in interacting quantum many-body systems. However, multicritical points predicted by theory have been rarely verified experimentally; finding multicritical points with specific behaviors and realizing their control remains a challenging topic. Here, we propose a system that a quantized light field interacts with a two-level atomic ensemble coupled by microwave fields in optical cavities, which is described by a generalized Dicke model. Multicritical points for the superradiant quantum phase transition are shown to occur. We determine the number and position of these critical points and demonstrate that they can be effectively manipulated through the tuning of system parameters. Particularly, we find that the quantum critical points can evolve into a Lifshitz point (LP) if the Rabi frequency of the light field is modulated periodically in time. Remarkably, the texture of atomic pseudo-spins can be used to characterize the quantum critical behaviors of the system. The magnetic orders of the three phases around the LP, represented by the atomic pseudo-spins, are similar to those of an axial next-nearest-neighboring Ising model. The results reported here are beneficial for unveiling intriguing physics of quantum phase transitions and pave the way towards to find novel quantum multicritical phenomena based on the generalized Dicke model.

1. Introduction

Critical phenomena is an everlasting subject of interest, both for its connection with the heart of statistical physics and for its relevance to everyday and technological applications [1]. A conceptual point intensely scrutinized focused on how quantum effects modify criticality and to chart quantum phase transitions [2].

In this line of research, a major topic is to characterize and study the quantum counterpart of multicritical points, which is a very active and promising field of research; see, e.g. [3]. In this field, it would be of paramount importance to have a physical setup, highly controllable, in which one can produce and control quantum multicritical points.

A major example of multicritical point is the Lifshitz point (LP) where three phases meet together, i.e. two first-order and a second-order (or two second-order and a first-order) phase transitions intersect in phase diagram. It was shown that the critical behavior around such a point can be achieved by varying the external parameters, and/or by preparing mixed compounds or alloys [4]. For instance, a paramagnetic phase, a (anti-)ferromagnetic phase and a helicoidal phase can meet at an LP, where the second order phase

transition line meshes with the first order one. LPs have been observed in a variety of condensed matter systems [5, 6] and expected to occur in systems of Rydberg atoms [7] and quantum chromodynamics [8, 9]. Quantum tricritical point (QTP) can be defined as a point where two lines of first-order and second-order phase transitions merge, with properties quite different from those at boundaries of conventional phase transitions. Remarkable efforts have been made on QTPs in various systems [10–12], and recently in Dicke models [13–16].

Dicke model describes typically the interaction between a quantized single-mode light field and an ensemble of two-level atoms [17–19], a many-spin version of a quantum Rabi model. In recent years many experimental works have been devoted to systems governed by such a model, including ones by optical cavities [20–22], circuit quantum electrodynamics (QED) [23] and cold atoms [24]. The Dicke model can exhibit second-order phase transition between superradiant phase (SP) and normal phase (NP) [25]. Due to the relative simplicity of theoretical approach, the Dicke model and its extension have become excellent platforms for studying quantum phase transitions, a useful path to simulate and understand the similar phenomena occurring in quantum many-body physics. Although various generalized schemes of Dicke model have been suggested [13, 14, 26–35], quantum multicritical behaviors predicted theoretically have not been verified by experiment. Hence, finding multicritical points with specific properties and realize their active control in such systems remains a challenging topic up to now.

In this work, we consider a driven system that can be described by an extended Dicke model, in which a laser field interacts with a gas of identical two-level atoms trapped in M cavities, with each cavity coupled by an arbitrary Zeeman (microwave) field. We show the emergence and manipulation of different quantum critical points (QCPs). Based on the relation between the order parameter of the radiance and system parameters, we propose a method to accurately determine the number and the positions of the QCPs in the phase diagram, which paves the way to manipulate the QCPs and to detailed study of the criticality in experimental realizations.

Furthermore, we explore the multicriticality of the system when the atom-field interaction is driven periodically by a laser field. In this case, the system can be described by a correlated model with spin–spin interaction between the cavities. Especially, the QCP can evolve into an LP when the driven is strong. Such a critical behavior is similar to that appearing in an axial next-nearest-neighboring Ising (ANNNI) model [6, 36] or quantum Lifshitz model [37], and the atomic pseudo-spins in each cavity represent the 'magnetic orders' of different phases around the LP.

Comparing with solid systems, the quantum critical behaviors predicted in the present system, together with its interesting physical properties, may be easier to observe and can be actively controlled experimentally due to highly tunable of the system.

2. Extended Dicke model

We consider a cold atom gas with N two-level atoms, which is trapped equally in M identical high-quality optical cavities and interacts with a quantized single-mode laser field. In each cavity, a microwave field couples the two states of the atoms, with coupling strength k_j for jth cavity ($j = 1, 2, \ldots, M$). These microwave fields serve as staggered Zeeman fields experienced by the atoms in the cavities, see appendix A for details.

The system can be described by an extended Dicke model ($\hbar \equiv 1$) by the Hamiltonian $H = H_{\mathrm{DM}} + H_{\mathrm{EF}}$, with

$$H_{\mathrm{DM}} = \omega a^{\dagger} a + \sum_{i=1}^{N} \left[\frac{\delta}{2} \sigma_i^z + \frac{G(t)}{2\sqrt{N}} \left(a^{\dagger} + a \right) \sigma_i^x \right], \tag{1}$$

$$H_{\mathrm{EF}} = \frac{\omega}{2} \sum_{j=1}^{M} k_j \sum_{i=1}^{N/M} \sigma_{i+N(j-1)/M}^x, \tag{2}$$

where H_{DM} is the Dicke Hamiltonian; H_{EF} is contributed by the external microwave fields; $a^{(\dagger)}$ is the bosonic operator for the laser field with frequency ω; δ is the transition frequency between the two atomic levels; σ_i^{η} ($\eta = x, y, z; i = 1, 2, \ldots, N$) are Pauli matrices; and G representing the laser-atom coupling strength is the single-photon Rabi frequency of the laser field, which can be modulated in time by varying the amplitude of the laser field. The system can be taken to be composed of M subsystems, each containing N/M atoms. We assume, without loss of generality, that the Zeeman coupling strength k_j ($j = 1, 2, \ldots, M$) is real and can take different signs. This can be realized by choosing the relative phases of the microwave fields. For convenience, we take ω as energy unit, i.e. $\omega = 1$.

The multi-cavity (or cavities array) systems, possible to realize in experiments, have been studied to be closely related to strongly correlated systems [38], where each cavity acts as a site in a lattice. We note that too many cavities may be technically challenged, therefore only the systems with a few ($\leqslant 5$) cavities are calculated here. Especially, when the periodic driving is turn on, at most three cavities are considered.

3. Results

3.1. Critical points and phase diagram without driving

For completeness, we first consider the simple case of a constant coupling strength, $G(t) = g$. Assume that the photon number in the laser field is large, and a mean-field approximation $a \to \langle a \rangle$ is applied. In thermodynamic limit ($N \to \infty$), the functional of energy-per-atom is given by $F(\xi) = \xi^2/\nu - \sum_{j=1}^{M} \sqrt{\delta^2 + (\xi + k_j)^2}$ (see appendix B) , where $\xi = 2g \langle a \rangle / \sqrt{N}$, $\nu = 2g^2/M$ are the dimensionless order parameter and the laser-atom coupling strength, respectively. If $\xi = 0$ ($|\xi| > 0$), the system is in NP (SP). We use the set, $K = \{k_1, k_2, \ldots, k_M; k_j \in \mathbb{R}\}$, to represent different Zeeman couplings in different cavities. The ground-state property of the system depends on the choice of K. For instance, in the case of $K = \{-1, 1\}$ the corresponding term in the Hamiltonian reads $H_{EF} = -\frac{1}{2} \sum_{i=1}^{N/2} \sigma_i^x + \frac{1}{2} \sum_{i=1}^{N/2} \sigma_{i+N/2}^x$.

Figures 1(a)–(c) show the phase diagrams of three examples for taking three sets: K_3, K_4 and K_5, chosen respectively as $K_3 \equiv \{-1, 0, 1\}$, $K_4 \equiv \{-1.5, -0.5, 2, 3\}$, and $K_5 \equiv \{-2, -1, 0, 1, 2\}$, by minimizing the energy-per-atom in the system. We see that, with the increase of M (the number of the cavities), the number of minima of $F(\xi)$ (each minimum corresponds to an SP) is increased, and hence the number of the SP phases is also increased. Moreover, the phase diagram for the case of K_5 is similar to that of K_3. The former contains three SPs (i.e. SP-I, SP-II, SP-III) and two QCPs, while the later contains two SPs (i.e. SP-I, SP-II) and one QCP.

To explore the properties of the QCPs more clearly, we start by locating the QCP in the superradiant region in figure 1(a), which is at $(\delta, \nu) = (0.715, 1.139)$. Then, we fix the value of δ or ν, and study how the order parameter ξ evolves with the variable ν or δ around the QCP. For $\delta = 0.655, 0.715, 0.775$, three phase diagrams with respect to ν are shown in figures 2(a)–(c), respectively. When $\delta = 0.655$, it is clear that a first-order phase transition appears at $\nu = 1.12$ (figure 2(a)); when $\delta = 0.715$, at the QCP the second-order phase transition between two SPs, as a joint of the first-order phase transition for $\delta < 0.715$, occurs at $\nu = 1.139, \xi = 0.902$ (figure 2(b)) where the derivative of the curve diverges. For $\delta = 0.775$, only the phase transition between the NP and the SP appears, and the curve in the superradiant region becomes smooth (figure 2(c)). The same phenomenon occurs in the other three diagrams shown in figures 2(d)–(f), when fixing the value of $\nu = 1.109, 1.139, 1.169$, respectively.

From figure 2(b), we find that when δ is fixed, both the functions $\xi(\nu)$ and its inverse $\nu(\xi)$ are monotonic. The QCP is the stationary point and the inflection point of $\nu(\xi)$. These properties can be then used to find an analytical method to locate the QCPs in the phase diagram.
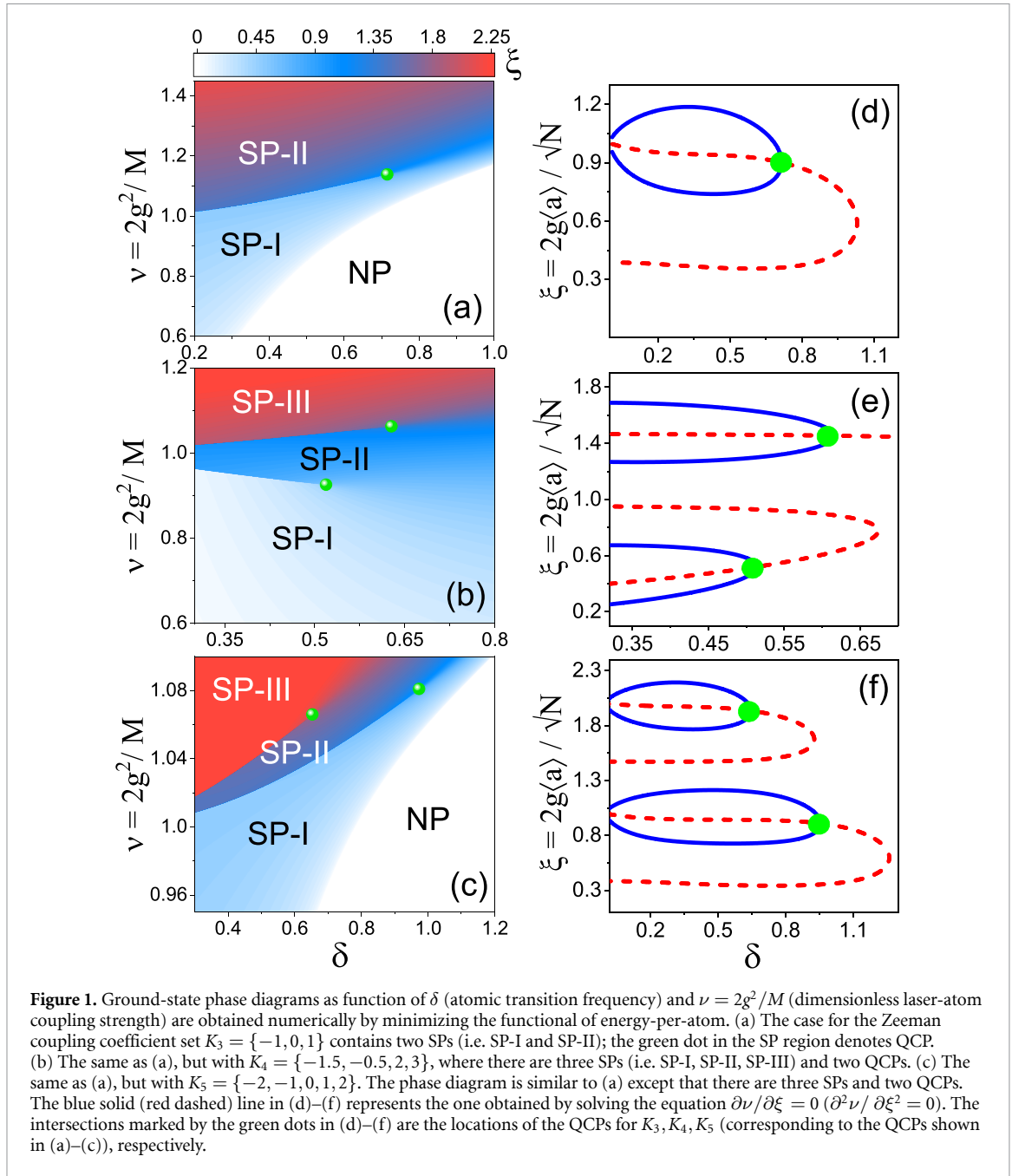
The positions of the QCPs in the phase diagrams figures 1(a)–(c) can be determined in the following way. First, let consider the condition of minimizing energy per atom $F(\xi)$, i.e. $\partial F(\xi)/\partial \xi = 0$, we can obtain the function ν, which is now a function of δ and ξ, i.e.

$$\nu = \nu(\delta, \xi) \equiv \frac{2\xi}{\sum_{j=1}^{M}(k_j + \xi)[\delta^2 + (k_j + \xi)^2]^{-1/2}}. \tag{3}$$

The QCP at the second-order phase transition joining the first-order phase transition line, is the stationary point of the curve as shown in figure 2(b), i.e. $\xi'(\nu) = \infty$ and $\nu'(\xi) = 0$. Moreover, we find that the QCP is also the inflection point of $\nu(\xi)$, namely the curvature of $\nu(\xi)$ is zero at the QCP. Hence, we are able to establish the two equations

$$\frac{\partial \nu(\delta, \xi)}{\partial \xi} = 0, \quad \frac{\partial^2 \nu(\delta, \xi)}{\partial \xi^2} = 0, \tag{4}$$

to find out the solutions (δ, ξ). Then, we put the solutions back to $\nu(\delta, \xi)$, and we obtain where the QCPs are. Note that we need to check whether the energy functional is a minimum at the intersection point, i.e. $\partial^2 F/\partial \delta^2 > 0$ or $\partial^2 F/\partial \nu^2 > 0$. However, equation (4) do not necessarily have solution, which depends on the coupling strengths K. For instance, no solution is found when $K = \{0, 1, 2\}$, since $\partial \nu/\partial \xi > 0$. The number and location of the QCP can be manipulated by tuning the external fields K to some extent. Moreover, knowing where the location of the QCP is also helpful to determine physical quantities such as the coupling strength g (related to ν) or the energy gap δ.

Figure 1. Ground-state phase diagrams as function of δ (atomic transition frequency) and $\nu = 2g^2/M$ (dimensionless laser-atom coupling strength) are obtained numerically by minimizing the functional of energy-per-atom. (a) The case for the Zeeman coupling coefficient set $K_3 = \{-1, 0, 1\}$ contains two SPs (i.e. SP-I and SP-II); the green dot in the SP region denotes QCP. (b) The same as (a), but with $K_4 = \{-1.5, -0.5, 2, 3\}$, where there are three SPs (i.e. SP-I, SP-II, SP-III) and two QCPs. (c) The same as (a), but with $K_5 = \{-2, -1, 0, 1, 2\}$. The phase diagram is similar to (a) except that there are three SPs and two QCPs. The blue solid (red dashed) line in (d)–(f) represents the one obtained by solving the equation $\partial \nu / \partial \xi = 0$ ($\partial^2 \nu / \partial \xi^2 = 0$). The intersections marked by the green dots in (d)–(f) are the locations of the QCPs for K_3, K_4, K_5 (corresponding to the QCPs shown in (a)–(c)), respectively.

In figures 1(d)–(f) we show the results respectively for the Zeeman coupling sets K_3, K_4, and K_5. In the figure, the blue line and the red dashed line are obtained by equation (4). The intersections marked by the green dots are the locations of the QCPs, corresponding respectively to the QCPs in (a)–(c). In figure 1(d), only one intersection represents a QCP at $(\delta, \nu, \xi) = (0.715, 1.139, 0.902)$ for the $K_3 = \{-1, 0, 1\}$ model, consistent with the result marked by the green dot in figure 1(a). We also find the intersection points for K_4, K_5 models in figures 1(e) and (f), which are the same QCPs marked in figures 1(b) and (c), respectively. The number of the SP is increased generally when the number of the Zeeman couplings increases. This can be understood by the reason that an addition of new Zeeman couplings can bring a new symmetry breaking in the system. Furthermore, the number and the location of the QCP can be manipulated by tuning the external fields K. Knowing where the QCP is also helpful to determine physical quantities such as the coupling strength g or the energy gap δ.

3.2. Multicriticality with a periodic driving
We now turn to consider the case that the atom-field coupling is periodically driven [39], $G(t) = g + A\cos(\Omega t)$. If the driving frequency is so large that we can integrate out all the fast-varied effects, then the effective time-independent Hamiltonian can be obtained for $g, \omega, \delta \ll \Omega$ (see details in appendix D)

Figure 2. For the $K_3 = \{-1, 0, 1\}$ model, different curve forms before and after the QCP at $(\delta, \nu, \xi) = (0.715, 1.139, 0.902)$. (a)–(c) ν is fixed to be 1.139 and δ is varied. (d)–(f) δ is fixed to 0.715 while ν is varied. At the QCP, the second-order phase transitions occur between two different superradiant phases.
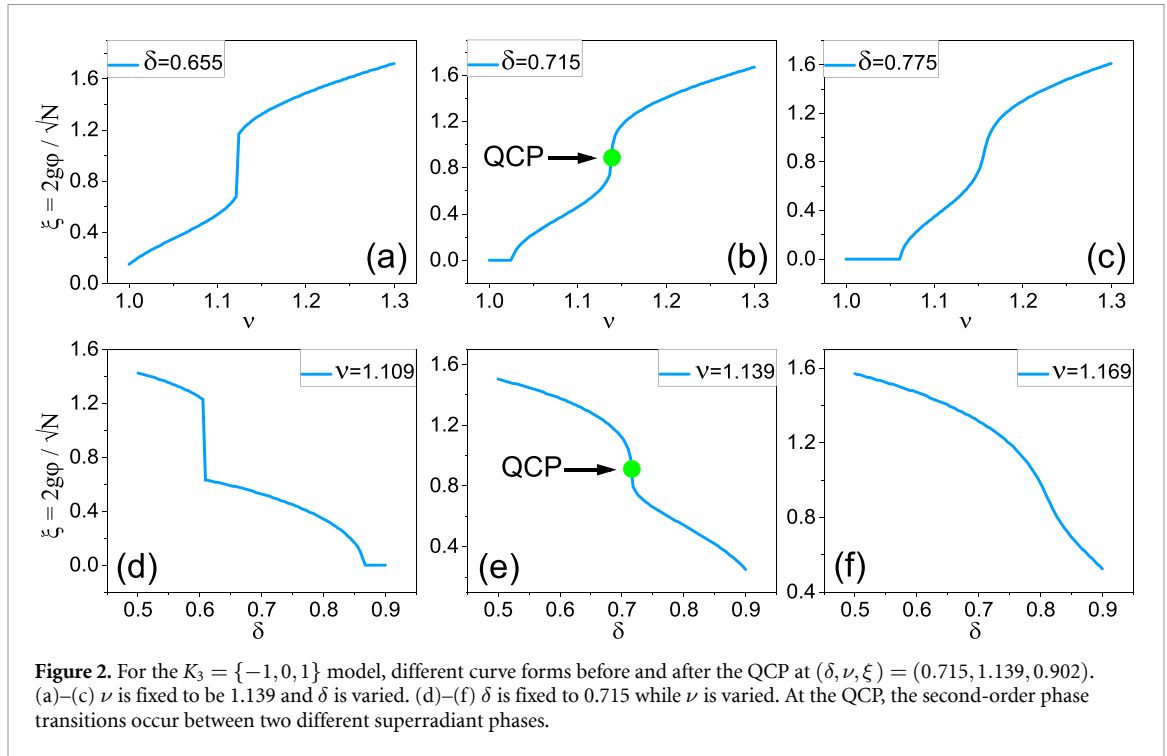
$$h_0 = \omega a^\dagger a + \frac{g(a^\dagger + a)}{\sqrt{N}} \sum_{j=1}^{M} J_j^x + \omega \sum_{j=1}^{M} k_j J_j^x + \frac{\omega}{2} \frac{A^2}{N\Omega^2} \left(\sum_{j=1}^{M} J_j^x \right)^2$$

$$+ \delta J_0 \left[\frac{2A(a^\dagger + a)}{\Omega\sqrt{N}} \right] \sum_{j=1}^{M} J_j^z, \tag{5}$$

where J_0 is the Bessel function of the first kind, $J_j^\mu = \frac{1}{2} \sum_i \sigma_{j+M(i-1)}^\mu$ are collective spin operators. This Hamiltonian is a combination of the anisotropic Zeeman couplings, the 'spin–orbit' coupling $(a + a^\dagger)J_j^{x,z}$ and the spin–spin interaction $J_i^x \cdot J_j^x$. All the couplings strengths can be conveniently changed in the highly tunable atomic systems comparing with the solid-state systems. If there is only one cavity, then no 'spin–spin' interaction is involved and the Hamiltonian goes back to that in [39].

In the thermodynamic limit, the fluctuation can be neglected and the energy of the ground state in the mean-field approach is obtained by substitutions in h_0: $J_j^z \rightarrow \frac{N}{2M} \left(Y_j^2 - 1 \right)$, $J_j^x \rightarrow -\frac{N}{2M} Y_j \sqrt{2 - Y_j^2}$, and $a \rightarrow \sqrt{N}X/\sqrt{2M}$ [40] (see appendix C). This energy functional is highly nonlinear and its minimum can only be found numerically. By minimizing the energy, the order parameters Y_j and $X = \sqrt{2M}\xi/(2g)$ and the phase of the ground state are obtained.

If there is no staggered Zeeman field, the phase transition is turned to first-order by the periodic driving at large δ (or large g [39]), and a QTP appears to join the second-order phase transition remaining at small δ. If the driving amplitude A is increased, the QTP moves in the direction of decreasing δ, until A is so large that all the phase transitions are first-order and the QTP disappears. In the following, for simplicity but without loss of generality, we focus on the several typical cases where two and three Zeeman fields are included.

Without the driving, the case of two staggered Zeeman fields, i.e. $K = \{-\epsilon, \epsilon\}$, leads a QTP joining the first-order phase transition (small δ) to the second-order phase transition (large δ). Increasing ϵ moves the QTP in the direction of increasing δ [13]. If both the driving and the Zeeman fields $K = \{-\epsilon, \epsilon\}$ ($\epsilon = 1$) jointly influence the system, the phase diagram (figure 3(a)) can be understood as the superposition of the phase diagrams with the driving only or with the staggered Zeeman fields only (details can be found in appendix C): at small δ, the first-order phase transition is led by the superposition of the first-order (from staggered Zeeman fields) and the second-order (from the driving) phase transitions; when δ is large, the opposite occurs; in the intermediate region of δ, the superposition of two second-order phase transitions remains the phase transition second-order. As shown in figure 3, the QTP at smaller δ is due to the staggered Zeeman fields while the QTP at larger δ is from the driving $A/\Omega = 0.23$. If the staggered Zeeman fields or the driving are increased, the two QTPs move towards each other as shown in figure 3(a), and finally all the phase transitions are first-order and the QTPs disappear once the two QTPs meet.
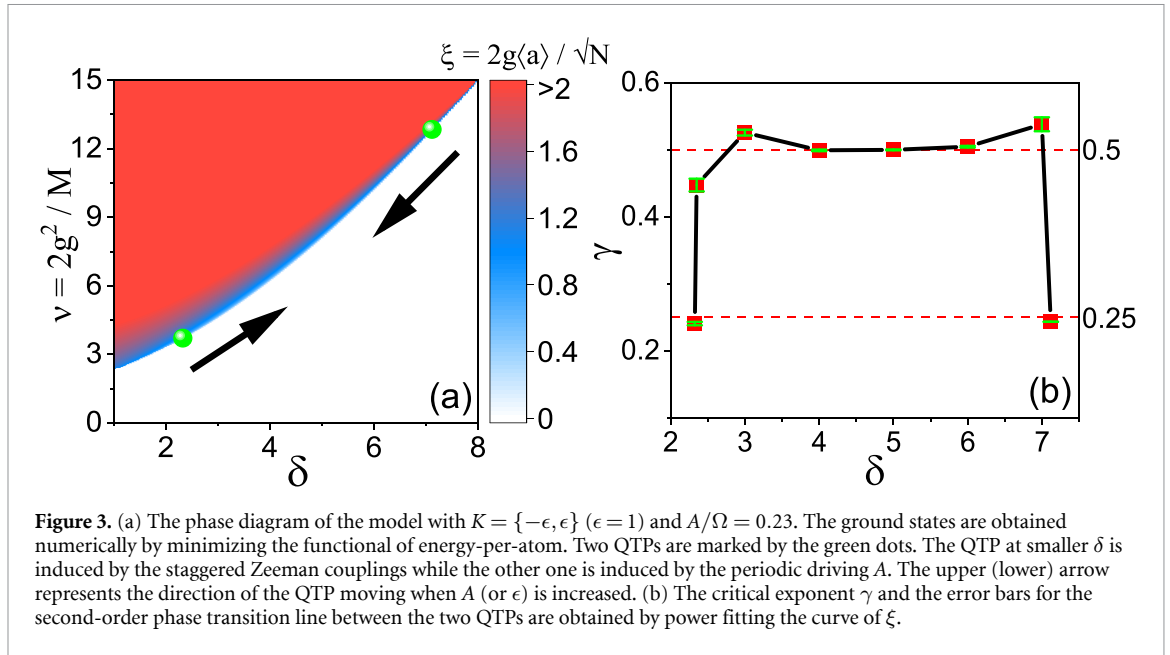
Figure 3. (a) The phase diagram of the model with $K = \{-\epsilon, \epsilon\}$ ($\epsilon = 1$) and $A/\Omega = 0.23$. The ground states are obtained numerically by minimizing the functional of energy-per-atom. Two QTPs are marked by the green dots. The QTP at smaller δ is induced by the staggered Zeeman couplings while the other one is induced by the periodic driving A. The upper (lower) arrow represents the direction of the QTP moving when A (or ϵ) is increased. (b) The critical exponent γ and the error bars for the second-order phase transition line between the two QTPs are obtained by power fitting the curve of ξ.

The critical exponents obtained by fitting the curve of the order parameter ξ (see the details in appendix D) are $\gamma = 0.25$ at the QTPs and $\gamma = 0.5$ for the second-order phase transition between the two QTPs.

3.3. LP in three-optical-cavity system

We next consider the three-cavity system with the periodic driving. For simplicity, we start by discussing the cases with the Zeeman couplings $K_3 = \{-1, 0, 1\}$. When the amplitude of the driving, A, is small, the phase diagram should be similar to that without driving shown in figure 1(a), a QCP, as the end point of the first-order phase transition line between the SP-I and SP-II, stays in the SPs to separate SP-I and SP-II. When A is increased, a QTP is generated at large δ ($\delta = 3.3$ for $A/\Omega = 0.3$) by the driving, as illustrated in figure 4(a). This QTP connects the first-order (for $\delta > 3.3$) and the second-order (for $\delta < 3.3$) phase transitions.

Increasing the amplitude of the driving pushes the QCP in the SP region towards the NP-SP transition in the direction of increasing δ (details can be found in appendix C), shown as the white arrow in figure 4(a). Meanwhile, the QTP is moved in the direction of decreasing δ by increasing A for the same reason as discussed in the two-cavity case (see also appendix C), as the black arrow shown in figure 4(a). When $A/\Omega > 0.35$, the QCP and the QTP can meet to form a new critical point.

As shown in figure 4(b), the SP-I does not disappear at weak coupling g, the first-order phase transition line between SP-I and SP-II is extended till the border of the NP-SP transition. The QCP which is the end of this phase transition line arrives at the NP-SP border and meet the QTP moving downwards along the NP-SP border. A LP is then formed, acting as a triple point that connects SP-I, SP-II and the NP. Two first-order phase transitions (one between the two SPs, the other between the NP and SP-II) and a second-order phase transition between the NP and SP-I intersect at the LP, as shown in figure 4(b). The SP-II has much stronger radiance than the SP-I, providing the feasibility to observe the LP by measuring the superradiance.

The periodic driving mostly affects the pseudo-spin polarized SP-II where the pseudo-spins of the three cavities are approximately parallel and its related phase transitions, since the spin–spin interaction is most significant when the pseudo-spins are polarized. The phase transition between spin unpolarized SP-I and NP is unchanged, since $\sum_j J_j^x$ is small and the spin–spin interaction is not important either. The reason why the LP appears can be traced from the Hamiltonian (5). Although the atoms do not explicitly interact with each other, the driven system is effectively governed by a spin–spin correlated model, which makes the system contain physics as rich as strongly correlated systems. Moreover, the effective Lagrangian of the system in the continuum approximation is in some sense equivalent to that of the quantum liquid system [37], which can be described by the quantum Lifshitz model containing the LP in the phase diagram. Hence, it would be reasonable that our system holds an LP.

This Hamiltonian is also similar to that of the ANNNI model [6, 36], in which the LP exists surrounded by (anti-)ferromagnetic, paraferromagnetic and modulated phases. In our case, the two SPs and the NP can also be characterized by the 'magnetic orders' of the pseudo-spins of the atoms in the three cavities. The
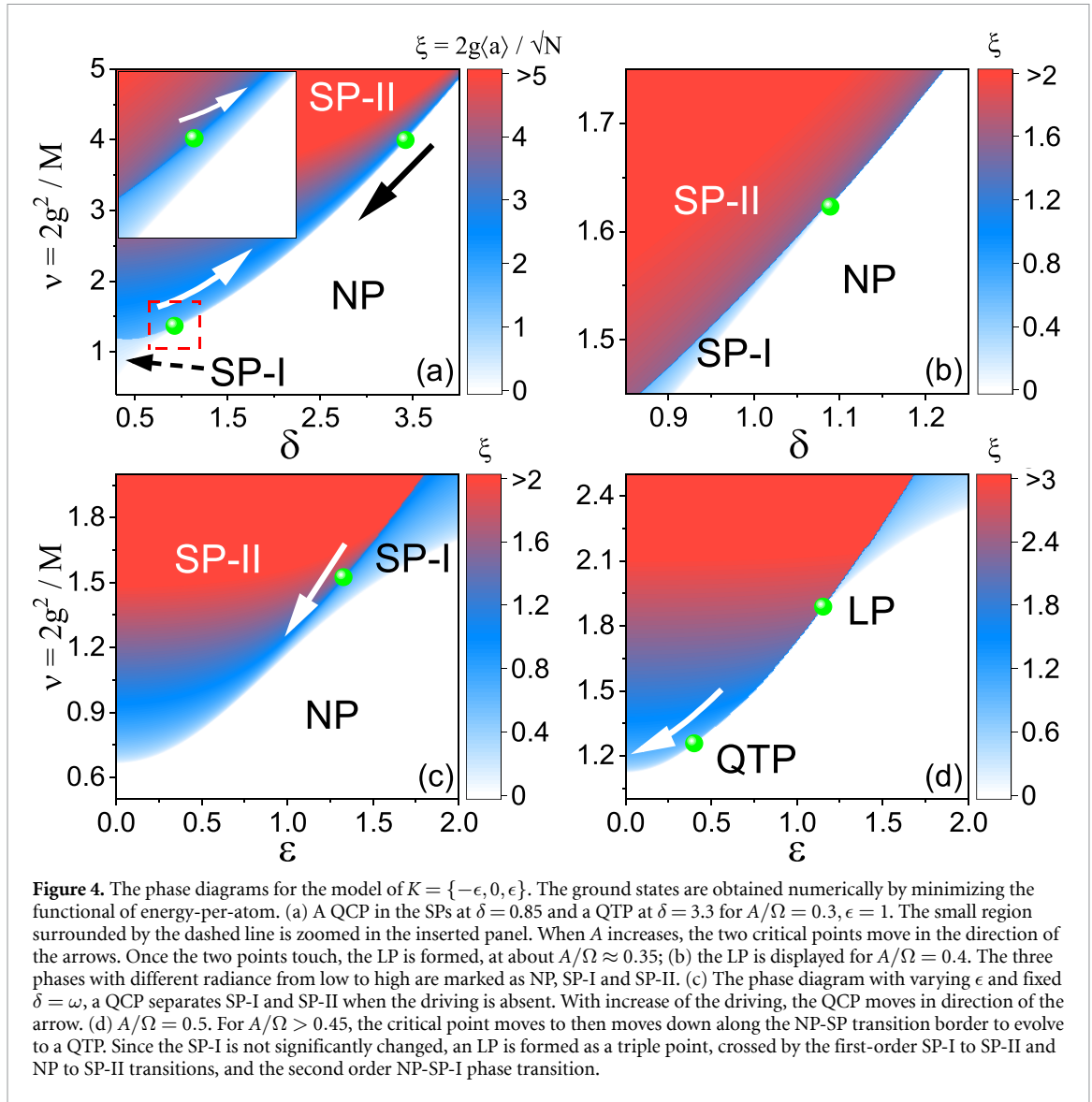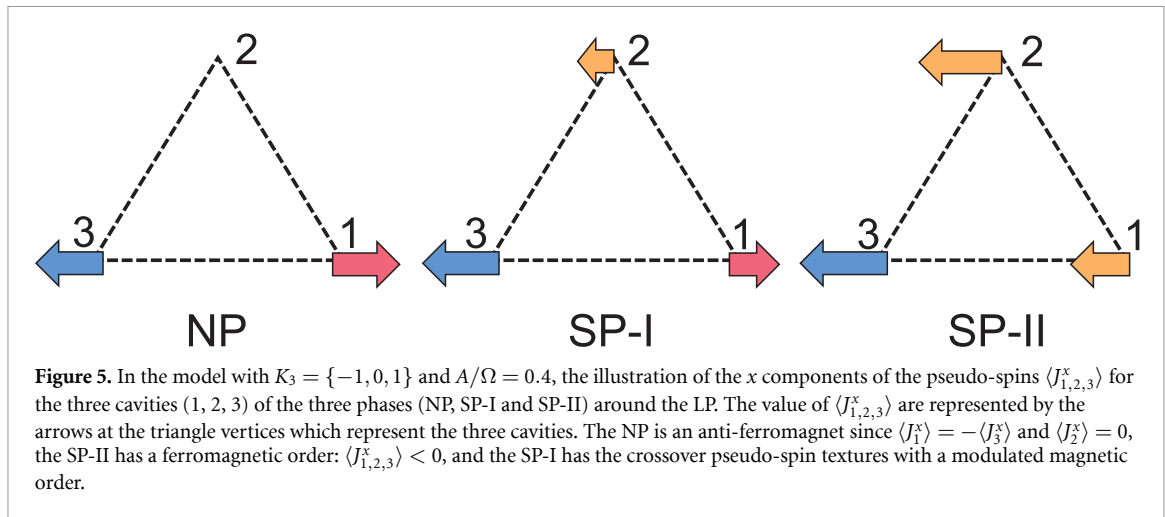
Figure 4. The phase diagrams for the model of $K = \{-\epsilon, 0, \epsilon\}$. The ground states are obtained numerically by minimizing the functional of energy-per-atom. (a) A QCP in the SPs at $\delta = 0.85$ and a QTP at $\delta = 3.3$ for $A/\Omega = 0.3, \epsilon = 1$. The small region surrounded by the dashed line is zoomed in the inserted panel. When A increases, the two critical points move in the direction of the arrows. Once the two points touch, the LP is formed, at about $A/\Omega \approx 0.35$; (b) the LP is displayed for $A/\Omega = 0.4$. The three phases with different radiance from low to high are marked as NP, SP-I and SP-II. (c) The phase diagram with varying ϵ and fixed $\delta = \omega$, a QCP separates SP-I and SP-II when the driving is absent. With increase of the driving, the QCP moves in direction of the arrow. (d) $A/\Omega = 0.5$. For $A/\Omega > 0.45$, the critical point moves to then moves down along the NP-SP transition border to evolve to a QTP. Since the SP-I is not significantly changed, an LP is formed as a triple point, crossed by the first-order SP-I to SP-II and NP to SP-II transitions, and the second order NP-SP-I phase transition.

pseudo-spins in each cavity are the sum of all the pseudo-spins of the atoms therein. The magnetic order of a phase in our system is represented by the textures of the pseudo-spins of the three cavities.

For simplicity, here we only monitor $\langle J_j^x \rangle$ in the three adjacent phases around the LP, and put $\langle J_j^z \rangle$ aside since it is not related to the spin–spin interaction or the anisotropic Zeeman couplings. Figure 5 clearly indicates the three different magnetic orders of the three phases: the NP has the anti-ferromagnetic order, SP-I has the modulated magnetic order, and SP-II is ferromagnetism. The full spin textures can be found in appendix E. We notice that if the pseudo-spin is more polarized, the atoms are more coherent, and the superradiance is stronger. The correspondence between the extended Dicke model and the ANNNI model illustrates why the atomic system can hold an LP surrounded by different magnetic orders. Besides, for the $K_3 = \{-1, 0, 1\}$ model without driving, the three phases (NP, SP-I and SP-II) also have these magnetic orders around the QCP. Namely, a Lifshitz regime including the QCP is perhaps already formed, which however cannot be closed up to an LP due to the lack of the driving induced spin–spin interaction.

To obtain more information of the evolution of the LP, we then consider the cases with varied microwave fields $K = \{-\epsilon, 0, \epsilon\}$ and a fixed energy between the two atomic levels $\delta = \omega$ to plot the phase diagram. Without driving, a first-order phase transition with its end QCP separating SP-I and SP-II is shown in figure 4(c). The strong staggered Zeeman couplings depolarize the atomic pseudo-spins to weaken the radiance. The SP-I with weaker superradiance thus appears at large ϵ. When the driving arises, the first-order phase transition line is extended and the QCP is also pushed towards the NP-SP transition line in the direction of decreasing ϵ (as the arrow in figure 4(c)).

When $A/\Omega \approx 0.4$, the phase transition line between the two SPs is extended to intersect with the NP-SP transition line. The QCP arrives at the NP-SP transition line to become an LP, which is intersected by the

Figure 5. In the model with $K_3 = \{-1, 0, 1\}$ and $A/\Omega = 0.4$, the illustration of the x components of the pseudo-spins $\langle J^x_{1,2,3} \rangle$ for the three cavities (1, 2, 3) of the three phases (NP, SP-I and SP-II) around the LP. The value of $\langle J^x_{1,2,3} \rangle$ are represented by the arrows at the triangle vertices which represent the three cavities. The NP is an anti-ferromagnet since $\langle J^x_1 \rangle = -\langle J^x_3 \rangle$ and $\langle J^x_2 \rangle = 0$, the SP-II has a ferromagnetic order: $\langle J^x_{1,2,3} \rangle < 0$, and the SP-I has the crossover pseudo-spin textures with a modulated magnetic order.

SP-I to SP-II first-order phase transition and two second-order phase transitions (NP to SP-I and NP to SP-II). The pseudo-spins of the three phases in the three cavities, $\langle J^x_{1,2,3} \rangle$, can also be illustrated by figure 5. If A continues to increase, the LP remains and a QTP is generated from the LP moving in the direction of decreasing ϵ along the NP to SP-II transition line (as the arrow in figure 4(d)). Meanwhile, the NP to SP-II phase transition between the LP and QTP turns to be first-order.

4. Conclusions and outlook

In the present study, we have proposed and investigated an extended Dicke model describing a laser-field interacting with an atomic gas trapped in cavities coupled by Zeeman fields. We have shown how to locate the QCPs, which can be manipulated through tuning the system parameters. We have demonstrated that, if the atom-field coupling is periodically driven, the system can be mapped to an interacting spin model and support rich critical behaviors. Especially, the critical point, close to the normal-SP transition, forms a Lifshitz regime and finally evolves to an LP around which the pseudo-spin of the atoms forms different magnetic orders due to the competition of the spin–spin interaction and anisotropic Zeeman couplings. The results reported here are also helpful for finding novel quantum multicritical phenomena in strongly interacting quantum many-body systems.

Given that the spin–spin interaction is long-range, thermalization is likely to be prevented in the system [41]. If the system is disordered by introducing noises in the external microwave fields or the driving, the many-body localization [42] may emerge and the energy levels of the system obey Poisson distribution with disorder [43]. Thereby, our system may be used to realize discrete time crystal [44] where pseudo-spins of the atoms would have spontaneous time translational symmetry breaking [45]. Moreover, it would be interesting to explore the effect of quantum fluctuations and consider the performance of metrological tasks near the quantum multicritical points based on the model suggested here.

Data availability statement

All data that support the findings of this study are included within the article (and any supplementary files).

Acknowledgments

Appendix A. Details on the experimental set-up

To obtain the extended Dicke model studied in the main text, we generalize the scheme used in [13]. We assume that a quantized single-mode laser field interacts with a cold atom gas, which is trapped equally in M identical high-quality optical cavities; see figure A1(a).

Figure A1. (a) Possible experimental setup for realizing the extended Dicke model. Atoms are trapped in *M* identical optical cavities, which are connected by single-mode fibers. (b) The excitation scheme of four-level atoms. An external laser (solid red lines), together with the dominant cavity mode (dashed red lines), drives Raman transitions between two ground-state sublevels $|0\rangle$ and $|1\rangle$ (i.e. pseudo-spin states). A microwave field is applied in each cavity to couple $|0\rangle$ and $|1\rangle$, with coupling strength *k*. The microwave fields are assumed to have relative phase differences, i.e. the sign of k_j ($j = 1, 2, \ldots, M$) can be changed actively, which served as effective Zeeman fields for different cavities.

The optical cavities are assumed to be connected by $M - 1$ optical fibers, each of them contains one normal mode that is near resonant with the atomic transition, and the other modes are negligible.

For the atoms in each cavity, only four levels (two upper and two lower ones) are involved. An external laser (represented by solid red lines), together with the dominant cavity-mode (represented by dashed red lines), drives the Raman transitions between two ground-state sublevels $|0\rangle$ and $|1\rangle$ (i.e. pseudo-spin states); see figure A1(b). In this way, each atom in the cavity may be described by a two-level model by using pseudo-spin language ($|0\rangle$ and $|1\rangle$ are two states of the pseudo-spin). Such a Raman excitation scheme can provide a strong coupling between the cavity-mode field and the atoms than that by using direct dipole excitation scheme, and hence is practical for the realization of the SP transitions.

Appendix B. Mean-field energy functional of the extended Dicke model without external driving

The mean-field Hamiltonian H_{MF} can be obtained by replacing the bosonic operator *a* with its expectation value $\varphi \equiv \langle a \rangle$. It is easy to obtain

$$H_{\mathrm{MF}} = \omega \varphi^2 + \sum_{i=1}^{N} \boldsymbol{B}_i \cdot \boldsymbol{\sigma}_i, \tag{B.1}$$

where $\boldsymbol{\sigma}_i = (\sigma_i^x, \sigma_i^y, \sigma_i^z)$, and

$$\boldsymbol{B}_i = \frac{\delta}{2}\hat{z} + \left(\frac{g\varphi}{M\sqrt{N}} + \frac{\omega}{2}k_i \right) \hat{x} \tag{B.2}$$

is the effective magnetic field experienced by *i*th atom.

The minimum energy of the system can be obtained by taking $\boldsymbol{B}_i$ to be all along the direction anti-parallel with $\boldsymbol{\sigma}_i$, i.e.

$$\langle H_{\mathrm{MF}} \rangle = \omega \varphi^2 - \sum_{i=1}^{N} |\boldsymbol{B}_i|. \tag{B.3}$$

So the mean-field energy per atom is given by

$$\frac{\langle H_{\mathrm{MF}}\rangle}{N} = \frac{\omega\varphi^2}{N} - \frac{1}{N}\sum_{i=1}^{N}\sqrt{\left(\frac{\delta}{2}\right)^2 + \left(\frac{g\varphi}{M\sqrt{N}} + \frac{1}{2}\omega k_i\right)^2}. \tag{B.4}$$

After substituting the dimensionless quantities ξ and ν into equation (B.4), we can obtain $F(\xi)$ in the manuscript.

Appendix C. Energy function in the models with periodic driving

We add both the external Zeeman fields and the time-dependent driven coupling to the Hamiltonian:

$$H(t) = \omega a^\dagger a + \delta\sum_{j=1}^{M}J_j^z + \frac{G(t)\left(a^\dagger + a\right)}{\sqrt{N}}\sum_{j=1}^{M}J_j^x + \omega\sum_{j=1}^{M}k_j J_j^x, \tag{C.1}$$

where the time dependent coupling is supposed to be

$$G(t) = g + A\cos\left(\Omega t\right),$$

with A and Ω being the amplitude and the frequency of the driving, respectively.

To eliminate the time-dependent terms we need to write the Hamiltonian in the interaction picture. Performing a canonical transformation

$$U = \prod_{j=1}^{M}\exp\left[-i\frac{A\left(a^\dagger + a\right)}{\sqrt{N}}\frac{\sin\left(\Omega t\right)}{\Omega}J_j^x\right]\exp\left(-i\omega' a^\dagger a t\right)\prod_{j=1}^{M}\exp\left(-i\delta' J_j^z t\right), \tag{C.2}$$

we have

$$H_{\mathrm{int}} = U^\dagger\left(H - i\frac{\partial}{\partial t}\right)U.$$

After this transformation we get the Hamiltonian

$$\begin{aligned}
H_{\mathrm{int}} = {}&\left(\omega - \omega'\right)a^\dagger a + i\omega\frac{A\sin\left(\Omega t\right)}{\sqrt{N}\Omega}\left(ae^{-i\omega't} - a^\dagger e^{i\omega't}\right)\sum_{j=1}^{M}\wp_j(t) + \omega\left[\frac{A\sin\left(\Omega t\right)}{\sqrt{N}\Omega}\right]^2\left[\sum_{j=1}^{M}\wp_j(t)\right]^2 \\
&+ \delta\sum_{j=1}^{M}\left\{J_j^z\left[J_0\ell(t)\right] + 2J_j^z\sum_{n=1}^{\infty}J_{2n}\left[\ell(t)\right]\cos\left(2n\Omega t\right) - \frac{J_j^+ e^{i\delta't} - J_j^- e^{-i\delta't}}{i}\sum_{n=0}^{\infty}J_{2n+1}\left[\ell(t)\right]\sin\left[(2n+1)\Omega t\right]\right\} \\
&+ \frac{g\left(a^\dagger e^{i\omega't} + ae^{-i\omega't}\right)}{\sqrt{N}}\sum_{j=1}^{M}\wp_j(t) + \omega\sum_{j=1}^{M}k_j\wp_j(t) - \delta'\sum_{j=1}^{M}J_j^z
\end{aligned} \tag{C.3}$$

where J_0, J_{2n}, J_{2n+1} are Bessel functions of the first kind, $J_j^+ + J_j^- = J_j^x$, $\frac{J_j^+ - J_j^-}{i} = J_j^y$, and

$$\ell(t) = \frac{2A\left(a^\dagger e^{i\omega't} + ae^{-i\omega't}\right)}{\Omega\sqrt{N}}, \tag{C.4}$$

$$\wp_j(t) = \frac{J_j^+ e^{i\delta't} + J_j^- e^{-i\delta't}}{2}. \tag{C.5}$$

When $g, \delta, \omega, \delta', \omega' \ll \Omega$ and $\delta', \omega' \to 0$, we can obtain the effective Hamiltonian $H_{\mathrm{eff}} \approx H_{\mathrm{int}}$, in the general form,

$$H_{\mathrm{eff}}(t) = \sum_{n=-\infty}^{\infty}h_n\exp\left(in\Omega t\right). \tag{C.6}$$

If the driving frequency is so large that we can neglect the fast oscillatory time dependence terms in the Hamiltonian, i.e. all $n \neq 0$ terms in equation (C.6), we find the time-independent effective Hamiltonian (with $\omega' = \delta' = 0$),

$$h_0 = \omega a^\dagger a + \frac{1}{2}\omega \left(\frac{A}{\sqrt{N}\Omega}\right)^2 \left(\sum_{j=1}^{M} J_j^x\right)^2 + \delta J_0 \left(\frac{2A\left(a^\dagger + a\right)}{\Omega\sqrt{N}}\right)\sum_{j=1}^{M} J_j^z$$

$$+ \frac{g\left(a^\dagger + a\right)}{\sqrt{N}}\sum_{j=1}^{M} J_j^x + \omega \sum_{j=1}^{M} k_j J_j^x, \tag{C.7}$$

which is shown in the main text. It in fact describes a system analogy to an anisotropic spin system interacting with a bosonic field. It also implies the possibility of different critical behaviors existing in its phase diagram. When $A = 0$ (without the driven term), the effective Hamiltonian becomes

$$h_0 = \omega a^\dagger a + \delta \sum_{j=1}^{M} J_j^z + \frac{g\left(a^\dagger + a\right)}{\sqrt{N}}\sum_{j=1}^{M} J_j^x + \omega \sum_{j=1}^{M} k_j J_j^x \tag{C.8}$$

which goes back to the original Hamiltonian.

In the thermodynamic limit, we again employ the Holstein–Primakoff transformation [40],

$$J_j^z = b_j^\dagger b_j - \frac{N}{2M}, \tag{C.9}$$

$$J_j^+ = b_j^\dagger \sqrt{\frac{N}{M} - b_j^\dagger b_j}, \tag{C.10}$$

$$J_j^- = \sqrt{\frac{N}{M} - b_j^\dagger b_j}\, b_j, \tag{C.11}$$

and introduce macroscopic displacements,

$$\langle a \rangle = c + X\sqrt{\frac{N}{2M}}, \langle b_j \rangle = d_j - Y_j\sqrt{\frac{N}{2M}}, \tag{C.12}$$

to obtain the mean-field energy by neglecting the small quantities $\sim O(1)$,

$$E_0 = \frac{N}{2M}\omega X^2 + \frac{\omega}{2}\left(\frac{A}{\sqrt{N}\Omega}\frac{N}{2M}\right)^2 \left(\sum_{j=1}^{M} Y_j\sqrt{2 - Y_j^2}\right)^2 + \frac{N}{2M}\delta J_0 \left(\frac{4AX}{\sqrt{2M}\Omega}\right)\sum_{j=1}^{M}\left(Y_j^2 - 1\right)$$

$$- \frac{N}{M}gX\sqrt{\frac{1}{2M}}\sum_{j=1}^{M} Y_j\sqrt{2 - Y_j^2} - \frac{N\omega}{2M}\sum_{j=1}^{M} k_j \left(Y_j\sqrt{2 - Y_j^2}\right). \tag{C.13}$$

At last, we obtain the effective energy function per atom

$$E_K = \omega X^2 + \frac{\omega}{4M}\left(\frac{A}{\Omega}\right)^2 \left(\sum_{j=1}^{M} Y_j\sqrt{2 - Y_j^2}\right)^2 + \delta J_0 \left(\frac{4AX}{\sqrt{2M}\Omega}\right)\sum_{j=1}^{M}\left(Y_j^2 - 1\right)$$

$$- 2gX\sqrt{\frac{1}{2M}}\sum_{j=1}^{M} Y_j\sqrt{2 - Y_j^2} - \omega \sum_{j=1}^{M} k_j \left(Y_j\sqrt{2 - Y_j^2}\right). \tag{C.14}$$

The order parameter defined in the main text ξ is related to the order parameter X here,

$$\xi = \frac{2g\langle a \rangle}{\sqrt{N}} = \frac{2gX}{\sqrt{2M}}. \tag{C.15}$$

For two staggered external fields, $K_2 = \{-1, 1\}$

$$E_{K_2} = \omega X^2 + \frac{\omega}{8}\left(\frac{A}{\Omega}\right)^2 \left(\sum_{j=1}^{2} Y_j\sqrt{2 - Y_j^2}\right)^2 + \delta J_0 \left(\frac{2AX}{\Omega}\right)\sum_{j=1}^{2}\left(Y_j^2 - 1\right)$$

$$- \sum_{j=1}^{2}(gX + \omega k_j)\left(Y_j\sqrt{2 - Y_j^2}\right), \tag{C.16}$$
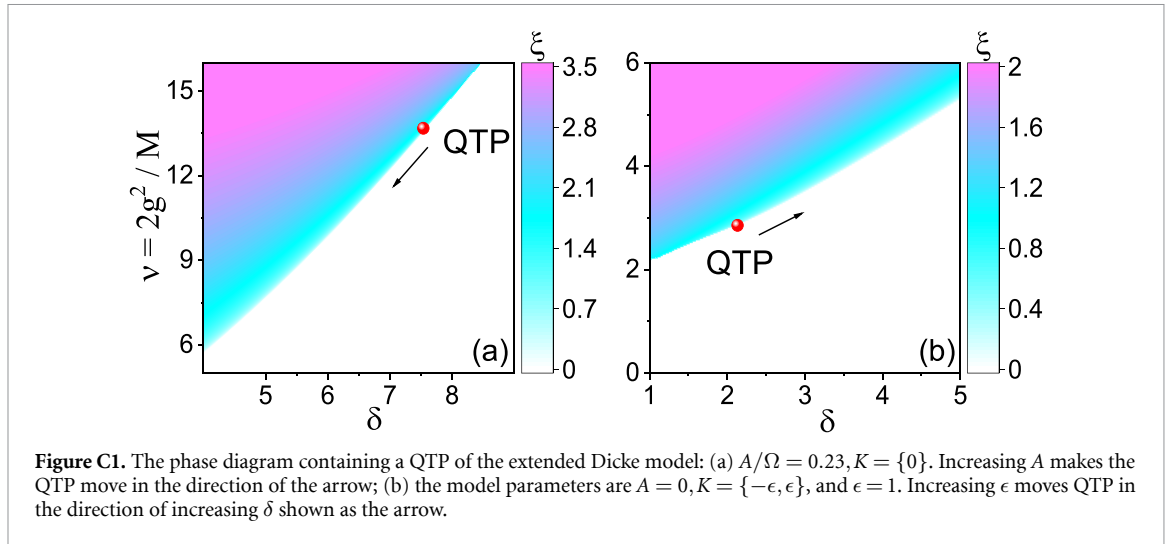
Figure C1. The phase diagram containing a QTP of the extended Dicke model: (a) $A/\Omega = 0.23, K = \{0\}$. Increasing A makes the QTP move in the direction of the arrow; (b) the model parameters are $A = 0, K = \{-\epsilon, \epsilon\}$, and $\epsilon = 1$. Increasing ϵ moves QTP in the direction of increasing δ shown as the arrow.
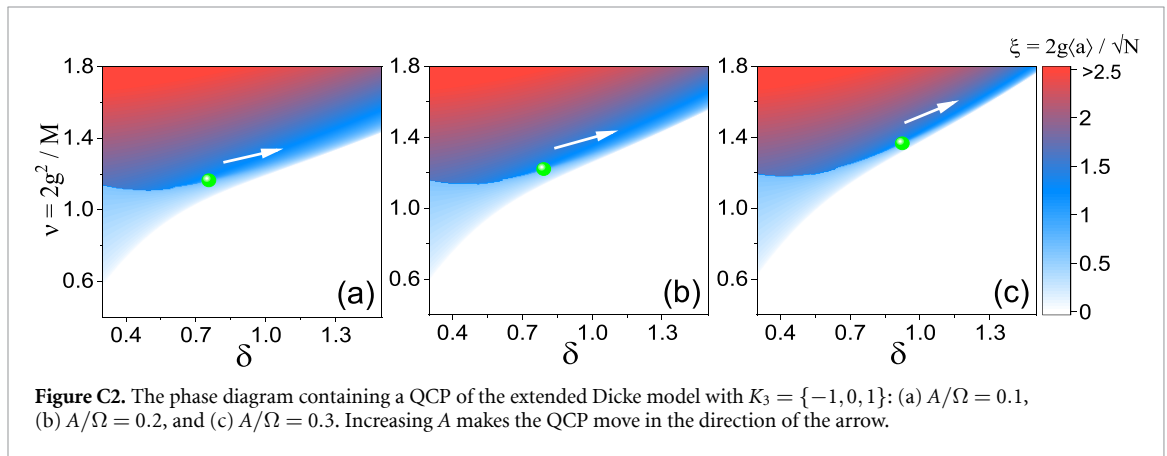

Figure C2. The phase diagram containing a QCP of the extended Dicke model with $K_3 = \{-1, 0, 1\}$: (a) $A/\Omega = 0.1$, (b) $A/\Omega = 0.2$, and (c) $A/\Omega = 0.3$. Increasing A makes the QCP move in the direction of the arrow.

with $k_1 = -1, k_2 = 1$. For three staggered external fields, $K_3 = \{-1, 0, 1\}$,
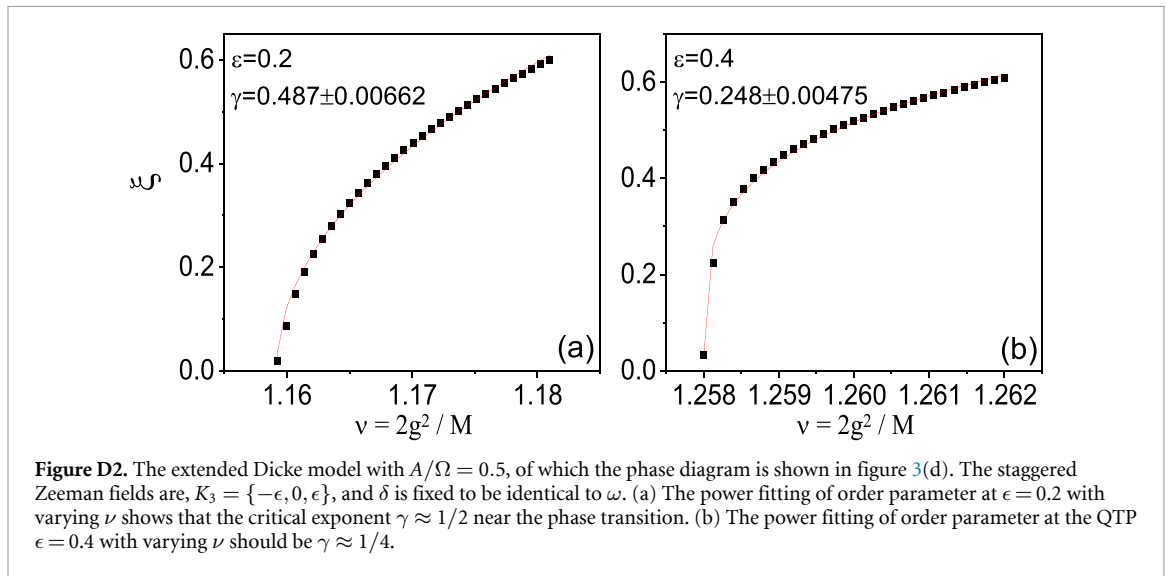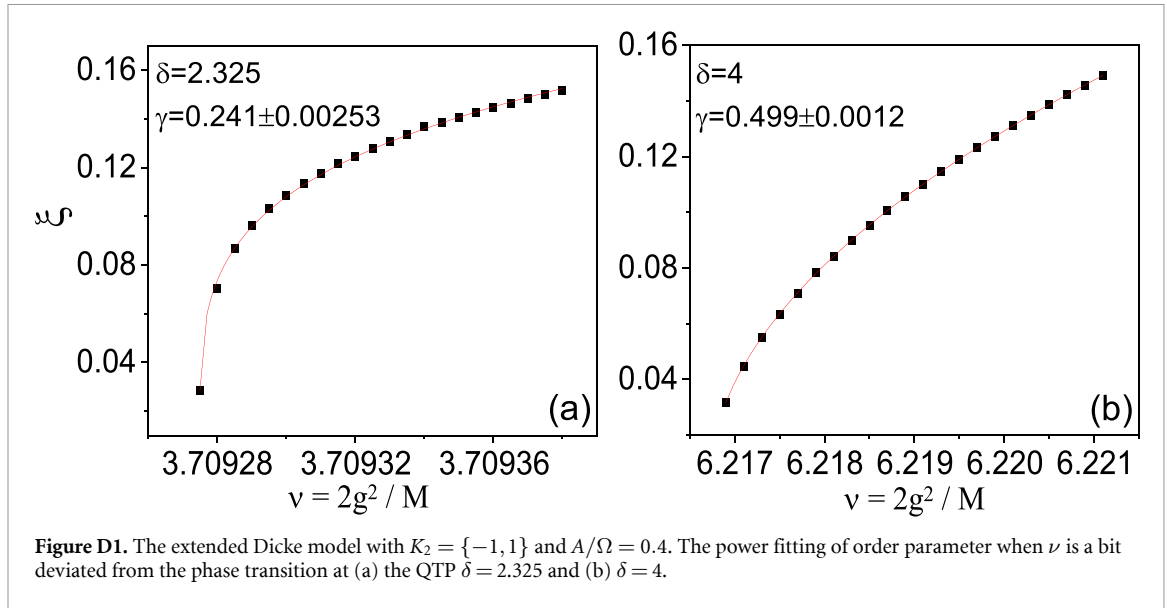
$$
E_{K_3} = \omega X^2 + \frac{\omega}{12}\left(\frac{A}{\Omega}\right)^2 \left(\sum_{j=1}^{3} Y_j \sqrt{2 - Y_j^2}\right)^2 + \delta J_0\left(\frac{4AX}{\sqrt{6}\Omega}\right)\sum_{j=1}^{3}\left(Y_j^2 - 1\right)
$$

$$
- \sum_{j=1}^{3}\left(\frac{2gX}{\sqrt{6}} + \omega k_j\right)\left(Y_j\sqrt{2 - Y_j^2}\right), \tag{C.17}
$$

with $k_1 = -1, k_2 = 0, k_3 = 1$.

By minimizing the energy function, we can find the order parameters $X = \frac{\sqrt{2M}\xi}{2g}$ and Y_j which are related to the atomic states. As mentioned in the main text, if there is no staggered Zeeman field, the driving can convert the second-order phase transition (between NP and SP) to the first-order one when δ is large. So a QTP appears to joint the first-order and the second-order phase transitions as shown in figure C1(a). If the driving A/Ω increases, the QTP moves in the direction where δ becomes small, as the arrow in figure C1(a).

If $A = 0$ and $K = 0$, the NP-SP phase transition is second-order. If $A = 0$ and $K = \{-\epsilon, \epsilon\}$ with $\epsilon = 1$, the QTP proposed in [13] is appearing as seen in figure C1(b). Nonzero ϵ makes the NP-SP phase transition be first-order when δ is small. If ϵ is increased, the QTP is pushed in the direction of increasing δ, as the arrow in figure C1(b). If both the driving and $K = \{-\epsilon, \epsilon\}$ are added in the system, when increasing either A or ϵ or increasing both of them, the QTP induced by the driving (or $K = \{-\epsilon, \epsilon\}$) are moving towards the other QTP (induced by K or the driving). When the two QTPs meet each other, all the phase transitions are first-order and no QTP appears any more.

In the case of $K_3 = \{-1, 0, 1\}$, the increase driving make the QCP in the superradiant region towards the NP-SP transition border in the direction of increasing δ. The movement of the QCP is shown as the arrows in figure C2.

Figure D1. The extended Dicke model with $K_2 = \{-1, 1\}$ and $A/\Omega = 0.4$. The power fitting of order parameter when ν is a bit deviated from the phase transition at (a) the QTP $\delta = 2.325$ and (b) $\delta = 4$.

Figure D2. The extended Dicke model with $A/\Omega = 0.5$, of which the phase diagram is shown in figure 3(d). The staggered Zeeman fields are, $K_3 = \{-\epsilon, 0, \epsilon\}$, and δ is fixed to be identical to ω. (a) The power fitting of order parameter at $\epsilon = 0.2$ with varying ν shows that the critical exponent $\gamma \approx 1/2$ near the phase transition. (b) The power fitting of order parameter at the QTP $\epsilon = 0.4$ with varying ν should be $\gamma \approx 1/4$.
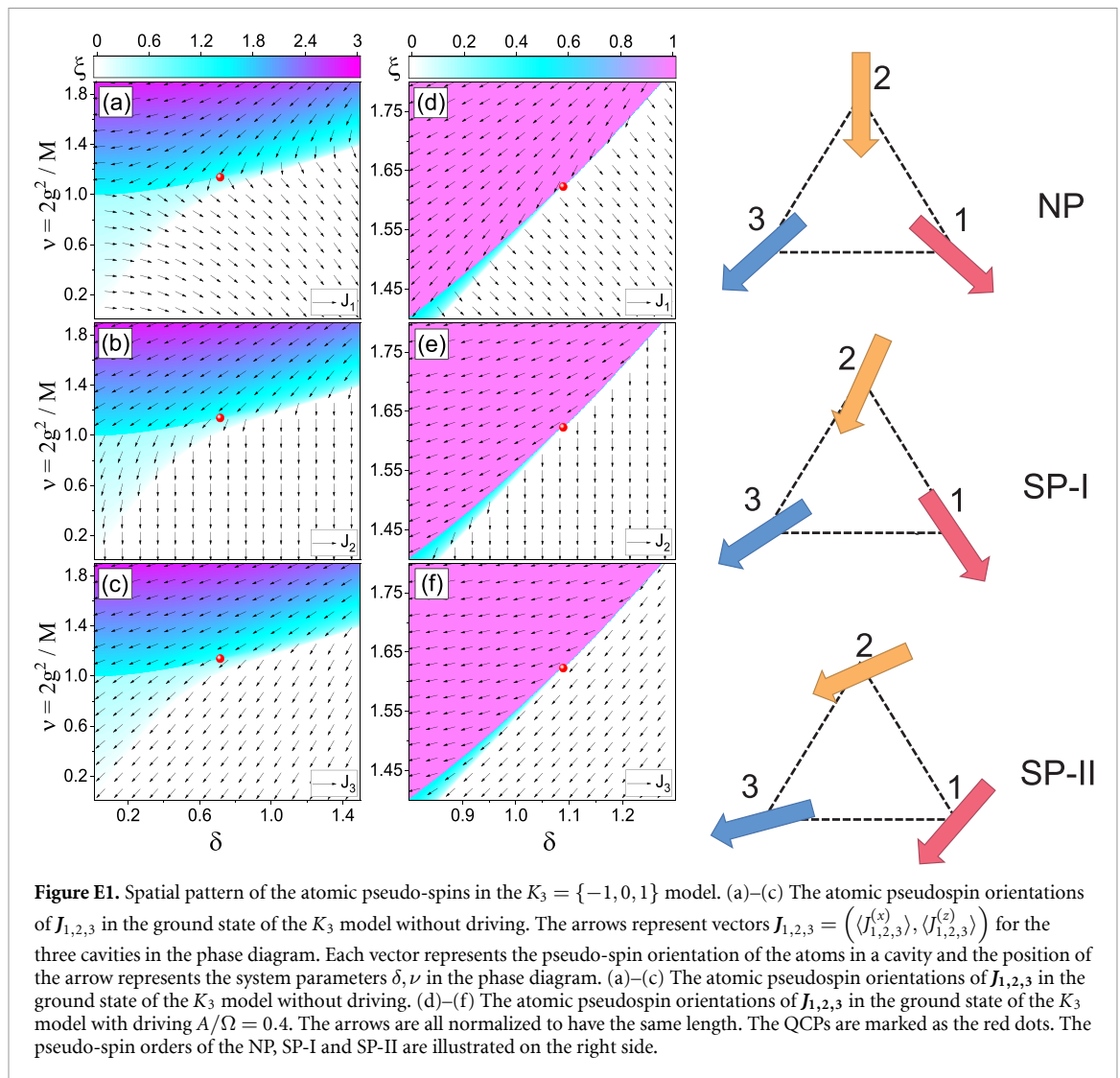
Appendix D. Critical exponents

We show here the data of the critical exponent γ, by power fitting, at the phase transition line of the model with $K_2 = \{-1, 1\}$ and $A/\Omega = 0.4$. In figure D1(a), the order parameter ξ is plotted when ν is slightly deviated from the phase transition at the QTP of $\delta = 2.325$. The power fitting gives the critical exponent $\gamma \approx 0.25$. At $\delta = 4$, the second-order phase transition with $\gamma \approx 0.5$ is shown in figure D1(b).

  Near the QTP in figure 3(d), in the main text, the critical exponent can also be found numerically by power fitting. In figure D2, we explicitly show the fitting data at the QTP to obtain that $\gamma \approx 1/4$.

Appendix E. Pseudo-spin textures and magnetic orders

We take the three-field model ($K_3 = \{-1, 0, 1\}$) as an example to illustrate the pseudo-spins of the atoms in different cavities. The pseudo-spins are represented by vectors in figure E1. The vectors is defined by $\boldsymbol{J}_{1,2,3} = \langle J_{1,2,3}^{(x)} \rangle \hat{\delta} + \langle J_{1,2,3}^{(z)} \rangle \hat{\nu} = \left(\langle J_{1,2,3}^{(x)} \rangle, \langle J_{1,2,3}^{(z)} \rangle \right)$. We note that the arrows represent the pseudo-spin of atoms $\boldsymbol{J}_i$ in the ith cavity, and the location of the arrow represents the parameters (δ and ν) in the phase diagrams. The atoms themselves are distributed randomly in the cavities.

  Without driving, the atoms pseudo-spins in three cavities are shown in figures E1(a)–(c), respectively. When $A/\Omega = 0.4$, the atoms pseudo-spins in three cavities are shown in figures E1(d)–(f), respectively. The illustrations of the ferromagnetic order of the NP, the paramagnetic order of the SP I and the anti-ferromagnetism in SP II are also shown in figure E1.

Figure E1. Spatial pattern of the atomic pseudo-spins in the $K_3 = \{-1, 0, 1\}$ model. (a)–(c) The atomic pseudospin orientations of $J_{1,2,3}$ in the ground state of the K_3 model without driving. The arrows represent vectors $J_{1,2,3} = \left(\langle J_{1,2,3}^{(x)} \rangle, \langle J_{1,2,3}^{(z)} \rangle \right)$ for the three cavities in the phase diagram. Each vector represents the pseudo-spin orientation of the atoms in a cavity and the position of the arrow represents the system parameters δ, ν in the phase diagram. (a)–(c) The atomic pseudospin orientations of $J_{1,2,3}$ in the ground state of the K_3 model without driving. (d)–(f) The atomic pseudospin orientations of $J_{1,2,3}$ in the ground state of the K_3 model with driving $A/\Omega = 0.4$. The arrows are all normalized to have the same length. The QCPs are marked as the red dots. The pseudo-spin orders of the NP, SP-I and SP-II are illustrated on the right side.

ORCID iD

Andrea Trombettoni ⓘ https://orcid.org/0000-0002-1108-4727

References

[1] Fisher M E 1984 Multicriticality: a theoretical introduction *Multicritical Phenomena* (Berlin: Springer)
[2] Sachdev S 2011 *Quantum Phase Transitions* (Cambridge: Cambridge University Press)
[3] As an example, see the interview to Fisher M E (available at: https://ipst.umd.edu/sites/default/files/documents/michaelefisher.pdf)
[4] Hornreich R M, Luban M and Shtrikman S 1975 Critical behavior at the onset of $\vec{k}$-space instability on the λ line *Phys. Rev. Lett.* **35** 1678
[5] Hornreich R M 1980 The Lifshitz point: phase diagrams and critical behavior *J. Magn. Magn. Mater.* **15-18** 387
[6] Diehl H W 2002 Critical behavior at M-axial Lifshitz points *J. Acta Phys. Slov.* **52** 271
[7] Chepiga N and Mila F 2021 Lifshitz point at commensurate melting of chains of Rydberg atoms *Phys. Rev. Res.* **3** 023049
[8] Buballa M and Carignano S 2015 Inhomogeneous chiral condensates *Prog. Part. Nucl. Phys.* **81** 39
[9] Pisarski R D, Skokov V V, Tsvelik A and Pedagogical A 2019 Introduction to the Lifshitz regime *Universe* **5** 48
[10] Beltz D, Kirkpatrick T R and Rollbühler J 2005 Tricritical behavior in itinerant quantum ferromagnets *Phys. Rev. Lett.* **94** 247205
[11] Misawa T, Yamaji Y and Imada M 2008 YbRh$_2$Si$_2$: quantum tricritical behavior in itinerant electron systems *J. Phys. Soc. Japan* **77** 093712
[12] Jakubczyk P, Bauer J and Metzner W 2010 Finite temperature crossovers near quantum tricritical points in metals *Phys. Rev.* B **82** 045103
[13] Xu Y and Pu H 2019 Emergent universality in a quantum tricritical Dicke model *Phys. Rev. Lett.* **122** 193201
[14] Zhu H-J, Xu K, Zhang G-F and Liu W-M 2020 Finite-component multicriticality at the superradiant quantum phase transition *Phys. Rev. Lett.* **125** 050402
[15] Xu Y, Padilla D F and Pu H 2021 Multicriticality and quantum fluctuation in a generalized Dicke model *Phys. Rev. A* **104** 043708
[16] Huang S, Liu N and Liang J-Q 2021 Quantum tricritical behavior and multistable macroscopic quantum states in generalized Dicke model *Results Phys.* **27** 104470
[17] Dicke R H 1954 Coherence in spontaneous radiation processes *Phys. Rev.* **93** 99

[18] Garraway B M 2011 The Dicke model in quantum optics: Dicke model revisited *Phil. Trans. R. Soc.* A **369** 1137

[19] Mandel L and Wolf E 1995 *Optical Coherence and Quantum Optics* (Cambridge: Cambridge University Press)

[20] Dimer F, Estienne B, Parkins A S and Carmichael H J 2007 Proposed realization of the Dicke-model quantum phase transition in an optical cavity QED system *Phys. Rev.* A **75** 013804

[21] Baumann K, Guerlin C, Brennecke F and Esslinger T 2010 The Dicke quantum phase transition with a superfluid gas in an optical cavity *Nature* **464** 1301

[22] Zhang Z Q, Lee C H, Kumar R, Arnold K J, Masson S J, Grimsmo A L, Parkins A S and Barrett M D 2018 Dicke-model simulation via cavity-assisted Raman transitions *Phys. Rev.* A **97** 043858

[23] Houck A A, Türeci H E and Koch J 2012 On-chip quantum simulation with superconducting circuits *Nat. Phys.* **8** 292

[24] Ritsch H, Domokos P, Brennecke F and Esslinger T 2013 Cold atoms in cavity-generated dynamical optical potentials *Rev. Mod. Phys.* **85** 553

[25] Wang Y K and Hioe F T 1973 Phase transition in the Dicke model of superradiance *Phys. Rev.* A **7** 831

[26] Kirton P, Roses M, Keeling J and Torre E G D 2019 Introduction to the Dicke model: from equilibrium to nonequilibrium and vice versa *Adv. Quantum Technol.* **2** 1970013

[27] Wang Y-Z, He S, Duan L and Chen Q-H 2020 Rich phase diagram of quantum phases in the anisotropic subohmic spin-boson model *Phys. Rev.* B **101** 155147

[28] Baumann K, Mottl R, Brennecke F and Esslinger T 2011 Exploring symmetry breaking at the Dicke quantum phase transition *Phys. Rev. Lett.* **107** 140402

[29] Puebla R, Relaño A and Retamosa J 2013 Excited-state phase transition leading to symmetry-breaking steady states in the Dicke model *Phys. Rev.* A **87** 023819

[30] Soriente M, Donner T, Chitra R and Zilberberg O 2018 Dissipation-induced anomalous multicritical phenomena *Phys. Rev. Lett.* **120** 183603

[31] Fan J, Yang Z, Zhang Y, Ma J, Chen G and Jia S 2014 Hidden continuous symmetry and Nambu–Goldstone mode in a two-mode Dicke model *Phys. Rev.* A **89** 023812

[32] Lu X, Li Z-M, Mangazeev V V and Batchelor M T 2021 Hidden symmetry in the biased Dicke model *J. Phys. A: Math. Theor.* **54** 325202

[33] Li Z-M and Batchelor M 2021 Hidden symmetry and tunneling dynamics in asymmetric quantum Rabi models *Phys. Rev.* A **103** 023719

[34] Baksic A and Ciuti C 2014 Controlling discrete and continuous symmetries in 'Superradiant' phase transitions with circuit QED systems *Phys. Rev. Lett.* **112** 173601

[35] Defenu N, Donner T, Macrí T, Pagano G, Ruffo S and Trombettoni A Long-range interacting quantum systems (arXiv:2109.01063)

[36] Selke W 1988 The ANNNI model—theoretical analysis and experimental application *Phys. Rep.* **170** 213

[37] Po H C and Zhou Q 2015 A two-dimensional algebraic quantum liquid produced by an atomic simulator of the quantum Lifshitz model *Nat. Commun.* **6** 8012

[38] Greentree A D, Tahan C, Cole J H and Hollenberg L C L 2006 Quantum phase transitions of light *Nat. Phys.* **2** 856–61

[39] Bastidas V M, Emary C, Regler B and Brandes T 2012 Nonequilibrium quantum phase transitions in the Dicke model *Phys. Rev. Lett.* **108** 043003

[40] Holstein T and Primakoff H 1940 Field dependence of the intrinsic domain magnetization of a ferromagnet *Phys. Rev.* **58** 1098
Vogl M, Laurell P, Zhang H, Okamoto S and Fiete G A 2020 Resummation of the Holstein-Primakoff expansion and differential equation approach to operator square roots *Phys. Rev. Res.* **2** 043243

[41] Sugimoto S, Hamazaki R and Ueda M 2022 Eigenstate thermalization in long-range interacting systems *Phys. Rev. Lett.* **129** 030602

[42] Nandkishore R and Huse D A 2015 Many-body localization and thermalization in quantum statistical mechanics *Annu. Rev. Condens. Matter Phys.* **6** 15
Abanin D A, Altman E, Bloch I and Serbyn M 2019 Colloquium: many-body localization, thermalization and entanglement *Rev. Mod. Phys.* **91** 021001
Sierant P, Biedroń K, Morigi G and Zakrzewski J 2019 Many-body localization in presence of cavity mediated long-range interactions *SciPost Phys.* **7** 008

[43] Oganesyan V and Huse D A 2007 Localization of interacting fermions at high temperature *Phys. Rev.* B **75** 155111

[44] Else D V, Bauer B and Nayak C 2016 Floquet time crystal *Phys. Rev. Lett.* **117** 090402

[45] Hu Y, Abdulwahab M and Luo W (unpublished)